ADVANCED MATERIALS

Supporting Information

for *Adv. Mater.*, DOI: 10.1002/adma.201701171

Materials Nanoarchitecturing via Cation-Mediated Protein Assembly: Making Limpet Teeth without Mineral

*Tina Ukmar-Godec, Luca Bertinetti, John W. C. Dunlop, Aljaž Godec, Michal A. Grabiger, Admir Masic, Huynh Nguyen, Igor Zlotnikov, Paul Zaslansky, and Damien Faivre**

Supplementary Information to:

Materials nano architecturing via cation-mediated protein assembly: making limpet teeth without mineral

Method

Animals. Limpets were purchased from the Monterey Abalone Company (California, USA). The radulae were extracted from *M. crenulata*, placed on petri dishes in order to preserve a flat shape and placed in the freezer at -80°C until further use. For the analysis reported here, freshly defrosted radulae were thoroughly washed in 3 steps in order to remove all organic debris: (i) washed in water and gently brushed with an ultra-soft brush, (ii) immersed shortly in 1% SDS and (iii) washed again in water. The water content in the tooth is approx. 13 %and henceforth we will refer to the dehydrated material only.

Sample embedding and polishing. Mature radula sections were dehydrated by a series of increasing ethanol concentrations (30%, 50%, 70%, 80%, 90% and 100%) and embedded in polymethylmethacrylate (PMMA). The embedded samples were cut with a slow speed saw (Bühler Isomet Low Speed Cutter 1000), ground with silicon carbide paper of increasing grit sizes and finally polished using 3 and 1 µm particulate diamond slurries.

EDTA-treated samples. Before the dehydration and embedding the samples were treated with 200mM EDTA, 10mM Tris buffer at pH 5 at room temperature. EDTA treatment was carried for 4 days and every day the EDTA solution was exchanged. Afterwards the samples were analyzed with Raman spectroscopy, nanoindentation and EDX. Prior to nanoindentation

and EDX the samples were dehydrated and embedded as described in the paper for the untreated samples.

Optical imaging. Optical images of the mature end of the radula was carried out with a Cannon Powershot G1 digital camera.

Scanning electron microscopy (SEM). Micrograph of the mature section of the radula was obtained with Field emission SEM (FE-SEM, Supra35 VP, Carl Zeiss, Germany) operating at 10 kV and the micrographs of the broken mature tooth at 1 kV. In both cases secondary electron imaging mode was used. The embedded sample was then investigated with high-resolution SEM (HR-SEM, JEOL JSM7500F) operating at 2 kV and using backscattered electron imaging mode which enable to observe the compositional contrast. The samples were mounted on an SEM-sample holder with conductive carbon tape and sputtered with Pt. Even though the samples were sputtered with Pt we experienced extensive problems with charging. For this reason we examined the broken tooth with cryo SEM (HR-SEM, JEOL JSM7500F) as well operating at 2 kV. Note that as a sign of a dominantly organic composition of these phases, we needed to perform cryo-SEM to achieve magnifications allowing efficient and well resolved imaging of the fibrous structures inside the tooth. The beam otherwise damaged the sample already upon shorter irradiation.

Microbeam WAXS and SAXS. X-ray scattering experiments were performed on the embedded thin samples at the µ-spot beamline (Paris et al., 2007) at the BESSY II synchrotron radiation facility in Berlin (Germany). A beam energy of 15 keV (λ = 0.826 nm)

was defined using a multilayer monochromator. The beam was focused by a toroidal mirror and experiments were collected on the area detector (MarCCD 225, MarUSA, Evanston) situated approximately 325 mm away from the sample. The final beam size was defined by a pinhole of 30 μm and 10 μm diameter behind the sample. All measurements were calibrated using a quartz powder placed at the sample position. Details of the data analysis are described in SI, section S12.

Nanoindentation. Embedded and polished samples were measured with a UB1 nanoindentation instrument (Hysitron, Minneapolis, MN, USA). Full-map indentation tests were performed on transverse cross-sections using a Berkovich diamond tip at a peak force of 500 μ N. The load function consisted of a 5-second loading to 500 μ N, followed by a 15-second hold at that force, and then a 5-second unloading. The resulting indents in a grid array were measured ca. 10 μm apart.

The same indentation procedure was also performed on polished samples at 92% relative humidity with a TI950 nanoindentation instrument (Hysitron, Minneapolis, MN, USA) equipped with environmental control chamber (xSol, Hysitron, Minneapolis, MN, USA) and humidity generator (HGC30, DataPhysics Instruments, Filderstadt, Germany). The measurements in high humidity were performed to investigate the possible influence of sample dehydration. Details of the data analysis are described in SI, section S12.

Finite element (FE) analyses. 3D FE models of 952,221 tetrahedral elements were created by importing the segmented data of 4 teeth at different stages of wear into Amira 5.2 (Visage Imaging GmbH, Germany) to create 2D isosurfaces. These triangulated surfaces were then

imported into HyperMesh 13.0 (Altair Engineering Inc., USA), corrected for errors, and then meshed in 3D. Simulations were performed using linear elastic materials properties (Young's modulus E = 16 GPa and Poisson's ratio ν= 0.3) with the models being clamped at the bottom. Four load cases F1, F2, F3 and F4 with magnitude of 0.125 N were applied on the tooth tips (0.0125mm²).

Raman spectroscopy and imaging. Raman imaging was performed using a confocal Raman microscope (alpha300, WITec, Ulm, Germany) equipped with a frequency doubled Nd:YAG laser excitation (λ=532 nm) and a piezoscanner. The laser beam was focused on the sample through an objective (60X, NA = 0.8) with a spot size of 0.61*λ/NA. For imaging, an integration time of 0.3 s was used for acquisition and pixels were separated by 0.5 µm. The spectra were acquired using a CCD detector (DU401A-BV, Andor, UK) placed behind the spectrometer (UHTS 300; WITec). The ScanCtrlSpectroscopyPlus software (WITec) was used for measurements and WITec Project Plus for spectrum processing. The image in Fig. 2d was generated by plotting the unmixed spectral components using WitecProjectPlus integrated Non-negative matrix functionalization (NMF) analysis function.

Micro-tomography. Samples of mature teeth were imaged using a laboratory microCT (Skyscan 1172 lab CT, BrukerCT, Kontich, Belgium). Scans were performed using 50 keV, with an effective pixel size of 2 µm, 0.7 s exposure time. Details of the data reconstruction are described in the SI, section S10.

Scanning Acoustic Microscopy (SAM). The embedded and polished samples of the longitudinal and transverse cross-section of the teeth were measured with SAM instrument (KSISAM 2000 by Krämer Scientific Instruments, Herborn,Germany) in combination with the custom Software MATSAM developed by Q-BAM Laboratory (university of Halle Wittenberg) for the raw data acquisition. V(z)-scans were performed in steps of $\Delta z = 2\mu m$ using a lens frequency of 400 MHz (opening angle 52°). The scan field size of 360x450µm² was used with a scan resolution of 512x512 points. Deionized water served as the coupling medium. For the conversion of the voltage into reflectivity R, three reference materials (acrylic glass, quartz and gold) were measured prior and after the measurement of the samples on the same day. In addition the output voltage in defocus position was recorded. Details of the data analysis are described in SI, section S12.

Energy Dispersive Spectroscopy (EDS) mapping - element analysis: The embedded thin slices of the samples of the mature teeth in transverse and longitudinal cross-section were analysed with EDX. The samples were mounted on a SEM stub with conductive carbon paint (SPI Supplies) in order to obtain the best contact. Elemental composition maps were obtained with a Jeol JSM 7500F scanning electron microscope equipped with two Oxford X-Max 150 Silicon drift detectors. An accelerating voltage of 20 kV was used. To avoid charging, samples were carbon-coated prior to the investigation.

S1. Sample composition

The water content in the teeth is 7-10 % (by mass), determined by differential weighing before and after dehydration. The dry sample composition was estimated with a combination of EXD and Amino acid analysis (AAA). The AAA results were taken from our experiments reported in Ref.[1] Disregarding the carbon coating we could obtain the following estimate for the molar ratio N:O:(Mg + Ca)=0.68:1:0.02, where O and N are determined with an accuracy of ~50%. Moreover, according to EDX we also obtain the molar ratio Mg:Ca=1:0.75. From the AAA analysis we take the result for the total protein content in the sample, which was determined to be 3.678 mmol/g. The relative amino acid composition of the proteins was found to be: 82.1% Gly, 10% His, 5.4 % Pro, 0.3% Asp, 0.3% Glu, 0.475% Thr 1,425%. In addition, sample contains 47.6 μmol/g free glucosamine.

We further make a simplifying assumption that the dehydrated sample consists of chitin, free glucosamine, protein, Ca and Mg (which is reasonable according to our Raman and scattering results). Using the N:O:Mg:Ca ratio and the amino acid composition we obtain the following estimate for the total sample composition in terms of % of mass: 67 % chitin, 23 % Gly, 5.7 % His, 2.3 % Pro, 0.85 % glucosamine, 0.56 % Ser, 0.02 % Thr, 0.016 % Glu, 0.014 % Asp, 0.4 % Mg and 0.5 % Ca. In the estimate, we assumed that the remaining mass is chitin (in agreement with the Raman results) and neglected the presence of other ions/elements such as Cl, K and Na in estimating the chitin content.

Note that the molar amounts of Ca and Mg are ~0.12 mmol/g and ~0.16 mmol/g (estimated by EDX with a accuracy of ~ 50%), whereas the amounts of acidic residues is ~0.11 mmol/g Asp and ~0.15 mmol/g Glu (from amino acid analysis).

S2. Raman microscopy

S2.1. Detailed analysis of Raman data in Fig. 3

Confocal Raman microscopy revealed a quite uniform chemical composition comprising α-chitin and proteins, whereas according to expectations no signs of any mineral phase were detected. A representative Raman spectrum is shown in Fig. S2.1. In agreement with the results in Ref. [1], which revealed a protein composition strongly dominated by Gly (80 %), His (10 %) and Pro (5%), Raman bands due to these residues are the only ones discernible.

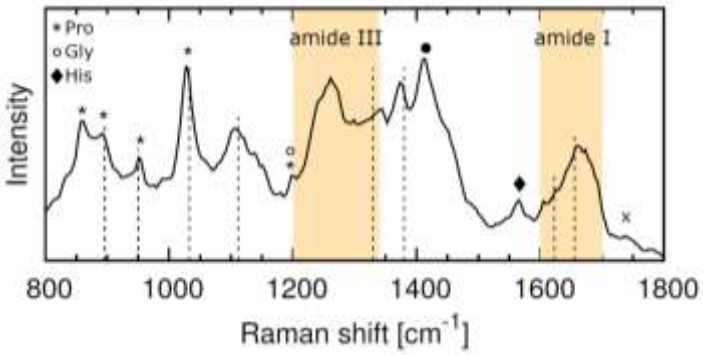

Fig S2.1: Average Raman spectra of raw teeth: The dashed lines denote peaks due to α-chitin fibers, full circle denotes the band due to CH and CH_2 deformations. The green bands at 1400-1454 cm^{-1} and 1620-1640 cm^{-1} denote the CN and backbone C=O stretch modes of Pro, respectively.[2]

The collected data was further analyzed with the Non-negative Matrix Factorization (NMF), which enables automatic un-mixing of spectral components and correlation with their distribution.[3] NMF identified two distinct kinds of spectra in the tooth tip differing in the protein bands (Fig. 3a), locally divided into an app. 15-20 microns thick shell and an inner core region (Fig. 3b). The shell region coincides with the outer parts of the Ca-rich region observed in EDX. More precisely, mostly the shell proteins have a higher fraction of β-sheets

than the core region, but the fraction of β-turns and/or disordered secondary motifs is also elevated,[4] which is shown in the highlighted bands in Fig. 3a. Differences are observed also in the CN stretching mode of Pro, which is sensitive to protein conformation[2] (green band in Fig. 3a). In particular, in the shell the band at higher wavenumbers (near 1450 cm^{-1}) is stronger, similar to trans-polyPro.[2] Moreover, the shell region also exhibits a shoulder in the region of CH and CH_2 deformations, which is a sign for elevated disordered and β-turn as well as β–sheet structural elements.[5] The most striking difference, however, was in the presence of an additional band at around 1740 cm^{-1} in the shell region (denoted by the arrow in lower panel of Fig. 3a), corresponding to ester groups.[4]

Interestingly, upon treatment with an EDTA solution, which partially removes the cations in a thin shell region (EDX results in S5 and Fig. S1.2 below), the relative fraction of disordered and β-turn motifs decreases (Fig. S1.2). Moreover, EDTA-treatment also induced a shoulder in the backbone C=O stretching band of Pro around 1623 cm^{-1} (Fig. S1.2).

S2.2. EDTA-treated samples

As compared to untreated samples the EDTA-treated teeth exhibited a lower fraction of disordered structure and β-turn motifs (see Fig. S2.2). Moreover, the His-band shifted towards smaller wavenumbers upon EDTA treatment (arrows in Fig. S2.2). Together with the extraction of Ca and Mg ions (Fig. S8) this suggests that some fraction of Ca and Mg ions might form a complex with His.[6] Moreover, the EDTA-treatment caused changes in the CN stretching mode of Pro, which is sensitive to protein conformation[2] (green band in Fig. S2.2). In particular, the band at higher wavenumbers (near 1450 cm^{-1}) developed a shoulder. The treatment with EDTA apparently did not cause any other significant changes in the spectrum. EDTA-treatment also induced a shoulder in the backbone C=O stretching band of Pro around

1623 cm^{-1}, which is a signature for an increased number of hydrogen-bonds in the backbone and a more extended chain[7].

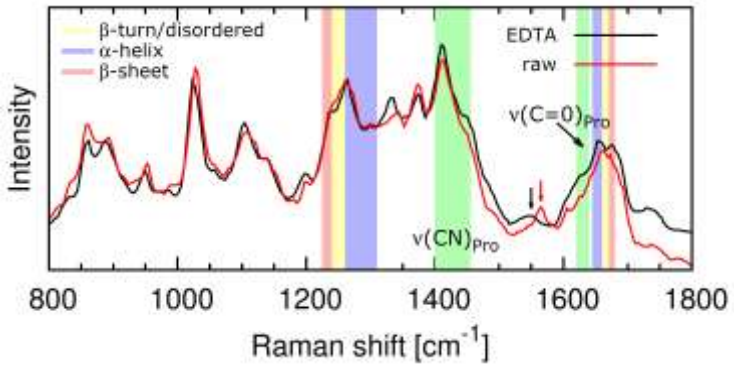

Fig S2.2: Average Raman spectra of raw and EDTA-treated teeth. The green band denote the CN and C=O stretching mode bands in Pro.

S3. Finite element modeling – functional analysis of the radular teeth and wear

Finite Element (FE) simulations shed light into the local stresses developed inside the tooth and tooth displacement upon applied a load to the tooth tip. In particular, we were interested in how wear affects the tooth functionality. As it is not known how exactly the tooth is loaded in-vivo we investigate four loading cases F1, F2, F3 and F4 with magnitude of 0.125 N (force taken according to Ref. 21) were applied on the tooth tips (0.0125mm^2) corresponding to different degrees of wear as depicted in Fig. S3.1.

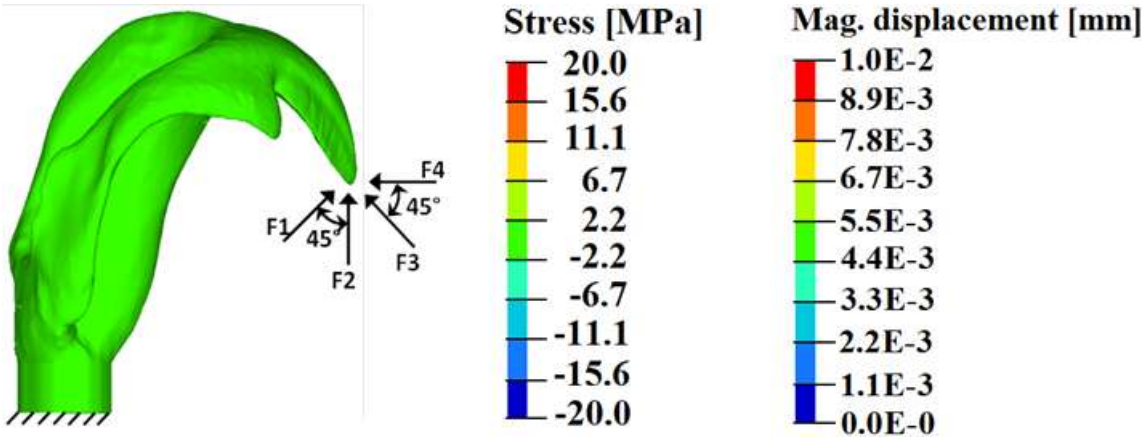

Fig S3.1: (left) 3D rendering of the tooth and schematics of the various loading directions considered in the FEM analysis; intensity scales for longitudinal stresses (center) and displacement magnitudes (right) corresponding to the results displayed in Tables S3.1-3.3.

In general FEM results reveal that the stresses inside the tooth depend on the direction of the load applied (see Tables S3.1 and S3.2 below). Moreover, the tooth appears to respond to the various stresses roughly equally well, demonstrating that the *M. crenulata* teeth represent a versatile harvesting tool.

The blunt rake-like leading area of worn teeth proves that wearing happens severely over there. The sharp hook-like shovel of unworn teeth is suitable for cutting and carrying food to mouth. The leading areas are not optimized for bending because the material in this area concentrates close to natural axis (Fig. S3.2 – Section C-C). In any load cases, bending stress in leading areas of worn teeth is small (Table 3.1).

On the contrary, the thin convex section of the middle part makes bending resistance of the tooth larger in leading-trailing direction (Fig. 3.2 – Section B-B). That effectively helps to reduce bending stress in the middle part of the tooth. The difference of stress in the middle part of worn teeth and unworn teeth is not considerable.

Table S3.1 Longitudinal Stress [MPa] – Section view.

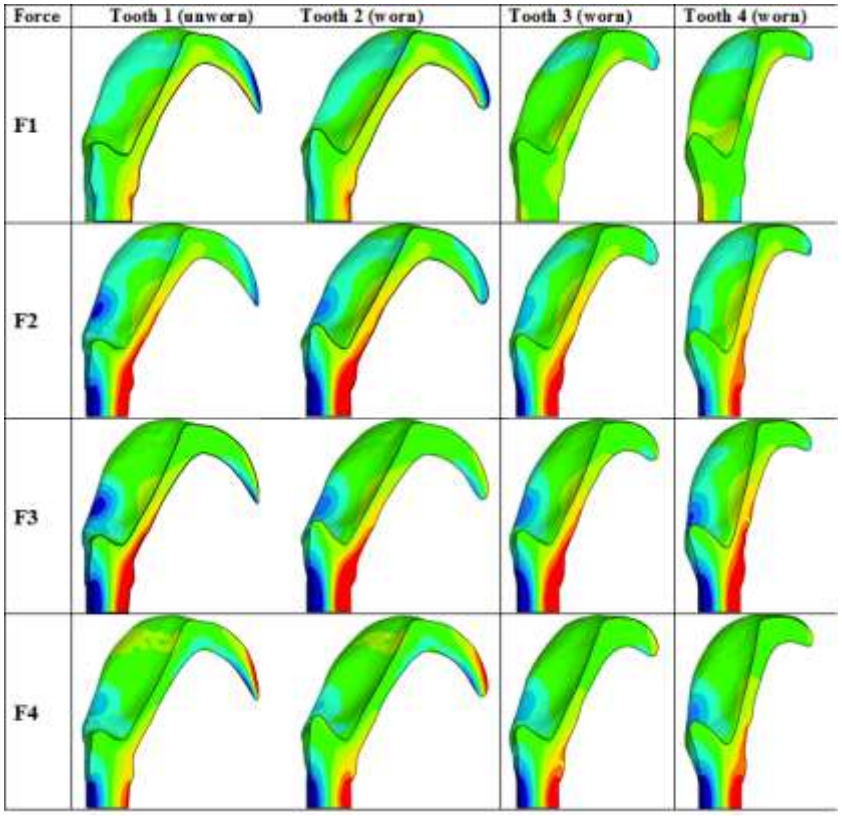

Table S3.2 Longitudinal Stress [MPa] – Perspective view.

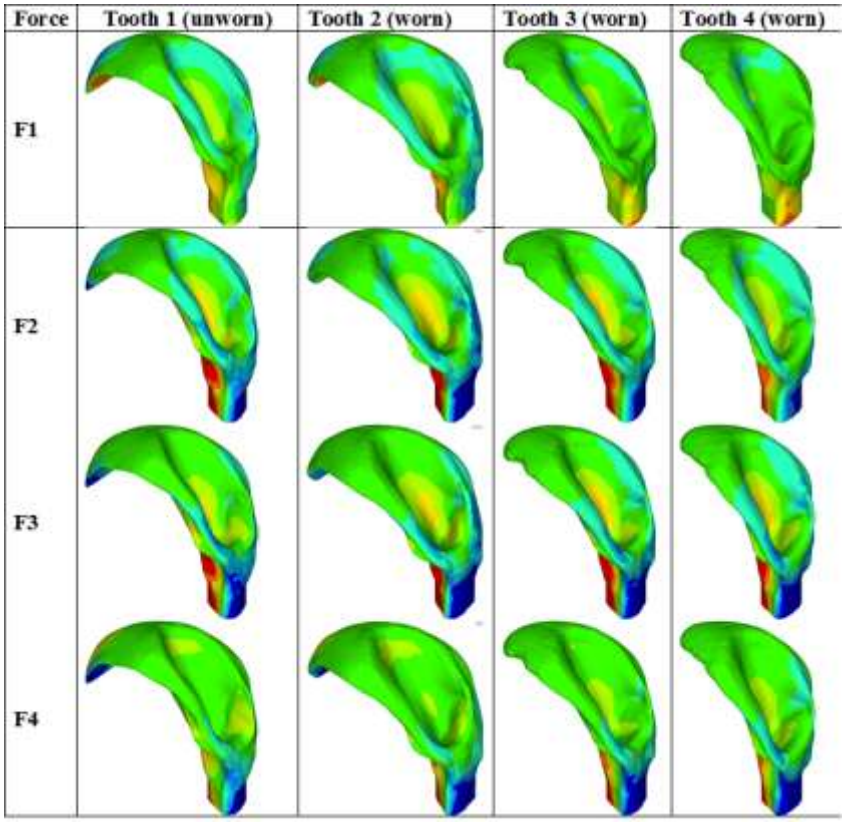

The shapes of the middle part and of the base part of the worn and unworn tooth are similar. It means these parts don't participate in scraping/cutting food. The relatively narrow but thick base part connects the tooth with the radular membrane (Fig. S3.2 – Section A-A). The maximum stress in the tooth is at base area. The reason for large stress in the tooth base is because of a small value of sectional modulus. This means that the morphology of the tooth base is not optimized for bending. But the small dimensions of the tooth base allow for constructing a compact radula with numerous rows of teeth.

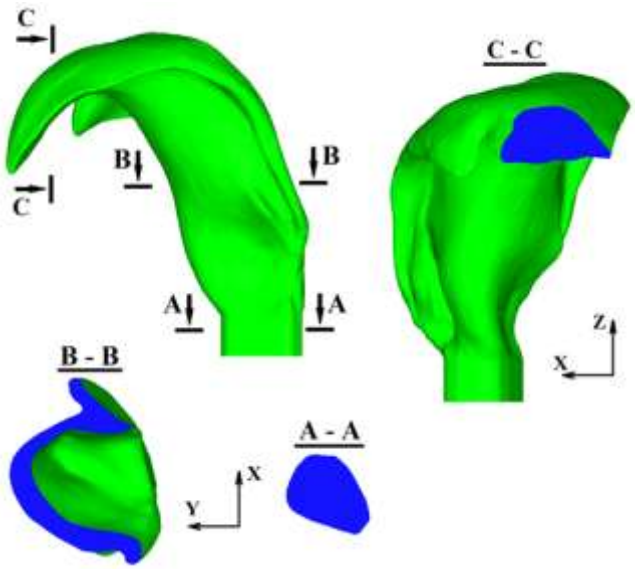

Fig S3.2: 3D rendering of the tooth and tooth sections.

In the load cases 1, 2 and 3 the leading area and middle part of the unworn teeth are displaced more than in worn teeth (see Table S.3.3). It means the unworn teeth are more flexible in feeding manipulation. On the contrary, in load case 4, the displacement of worn teeth is larger than the displacement of unworn teeth because the moment arm (distance between force and clamped area) of force applied on the worn teeth is larger.

Table S3.3 Displacement magnitude[mm] – Perspective view

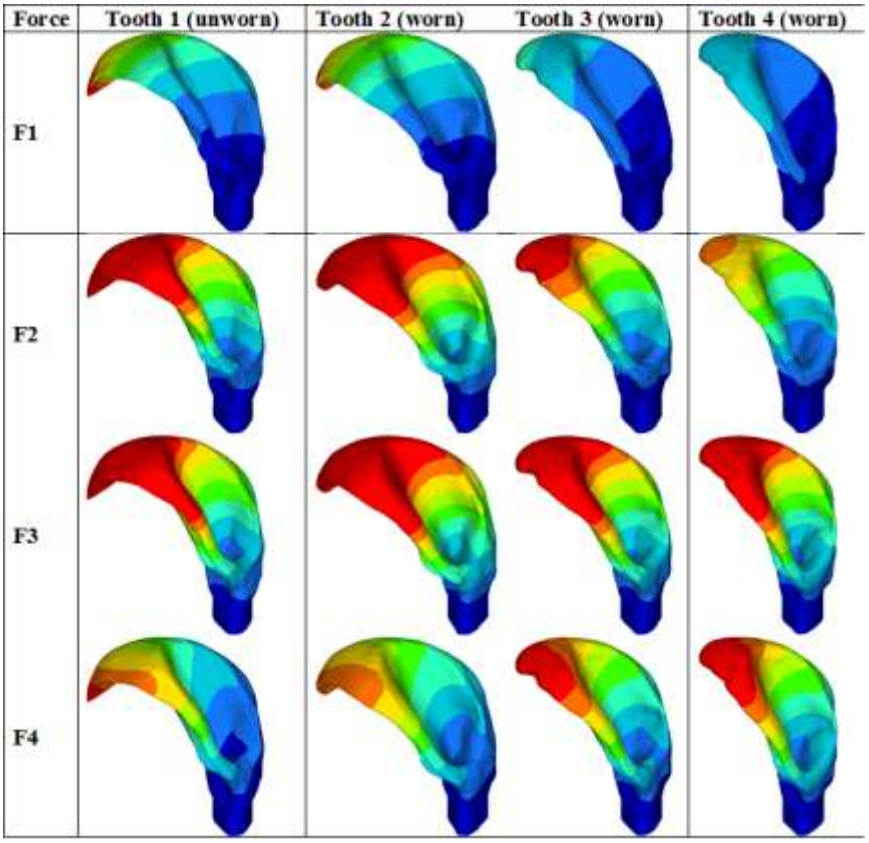

S4. Additional results: Nanoindentation at high humidity, Micro-tomography and scanning acoustic microscopy

To assess the effect of dehydration on the material stiffness additional experiments were performed at an elevated relative humidity of 92%. The results of 5 different measurements are shown in Fig. S4.1. We find that the stiffness is reduced at high relative humidity as a result of moisture uptake, but the observed stiffness profile appears to be rather similar to the one observed in dehydrated sections (compare with Fig. 1f). More importantly, the stiffness along the hydrated tooth is of the same order of magnitude, which is in stark contrast to the extreme variations in hydrated squid beaks.[22] We therefore conclude that while hydration certainly does affect the stiffness of tooth sections, the effect is not dramatic.

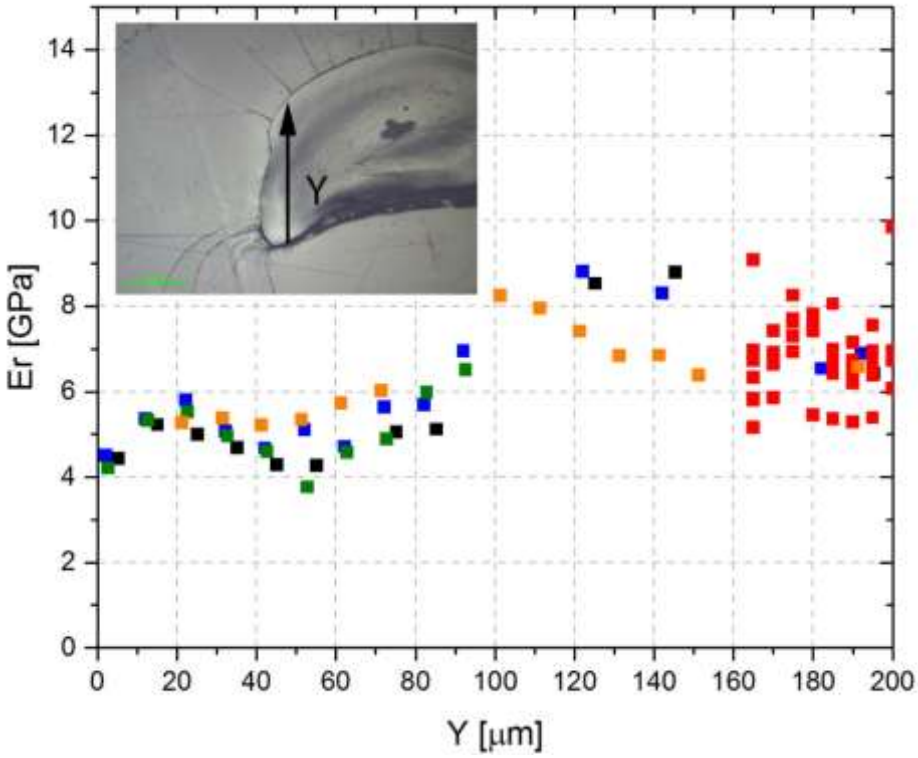

Figure S4.1: Supplementary nanoindentation at 92%RH. The reduced modulus profile obtained by 5 independent line-scans along the direction denoted by the arrow in the inset.

The µ-CT image in Fig. S4.2a readily depicts a shape-reserving wear (i.e., the wear pattern is asymmetric, such that the tooth tip appears to preserve sharpness). The acoustic reflectivity of longitudinal sections is depicted in Fig. S4.2b. Acoustic reflectivity depends on both the local mass density and the local modulus and therefore does not reflect the stiffness alone.[8] SAM results agree well with the nanoindentation results (Fig. 1e and 1f in the main text), revealing a slightly more reflective (i.e., stiffer and/or more dense) shell enclosing the less reflective (softer and/or less dense) core. As µ-CT did not reveal significant density variations inside the tooth we assume that SAM mostly reflects variations in stiffness.

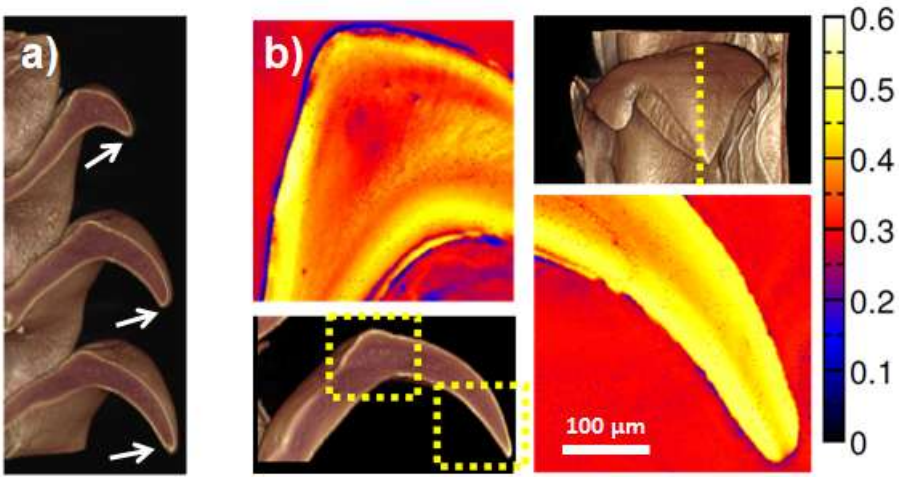

Figure S4.2: Supplementary micro-tomography and SAM. a) Micro-CT image of worn teeth depicting shape-preserving wear (arrows); b) Scanning acoustic micrograph of a longitudinal section of teeth.

S5. Characteristic 2-dimensional diffraction pattern observed inside the tooth

The typical scattering pattern is depicted in Fig. S5 and reveals peaks characteristic for crystalline α-chitin.[9-11] The fact that the reflections do not have a uniform intensity over the circle is indicative or preferential orientational alignment of the fibers. The reflections are assigned in the figure caption. Note that no reflections other than those corresponding to chitin were observed confirming that the teeth do not contain any mineral phases. The orientation of the chitin fibers was determined on the basis of the angular dependence of the (040) and (013) reflections.[9-11]

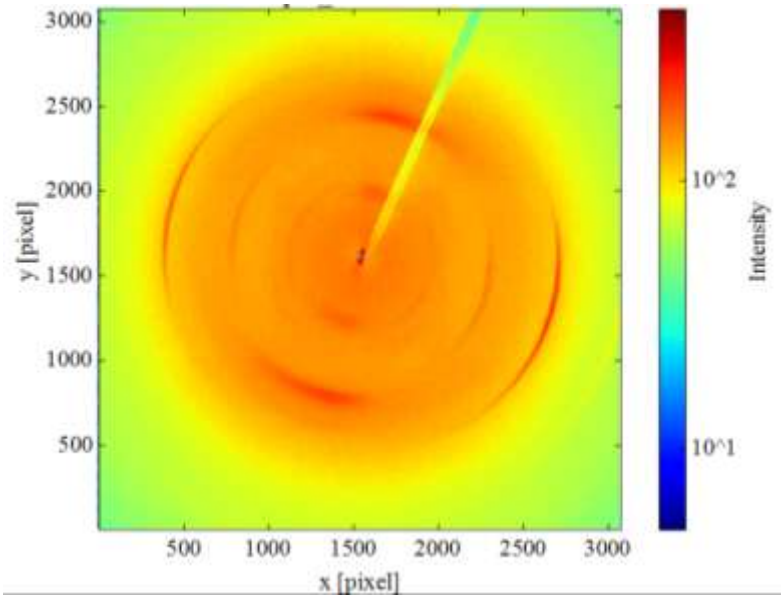

Fig. S5: Characteristic 2D diffraction pattern. The resolved reflections outward from the centre are assigned to (020), (021), (040) and (013), respectively.

S6. Wide-angle X-ray scattering analysis of the chitin fibre texture

The degree of orientational order was determined based on the peak to background ratio in the radially integrated angular scattering profiles and is shown in the left panel of Fig. S6. The in-plane as well as the out-of-plane (i.e. tilt) angle are shown in the right panel in Fig. S6.

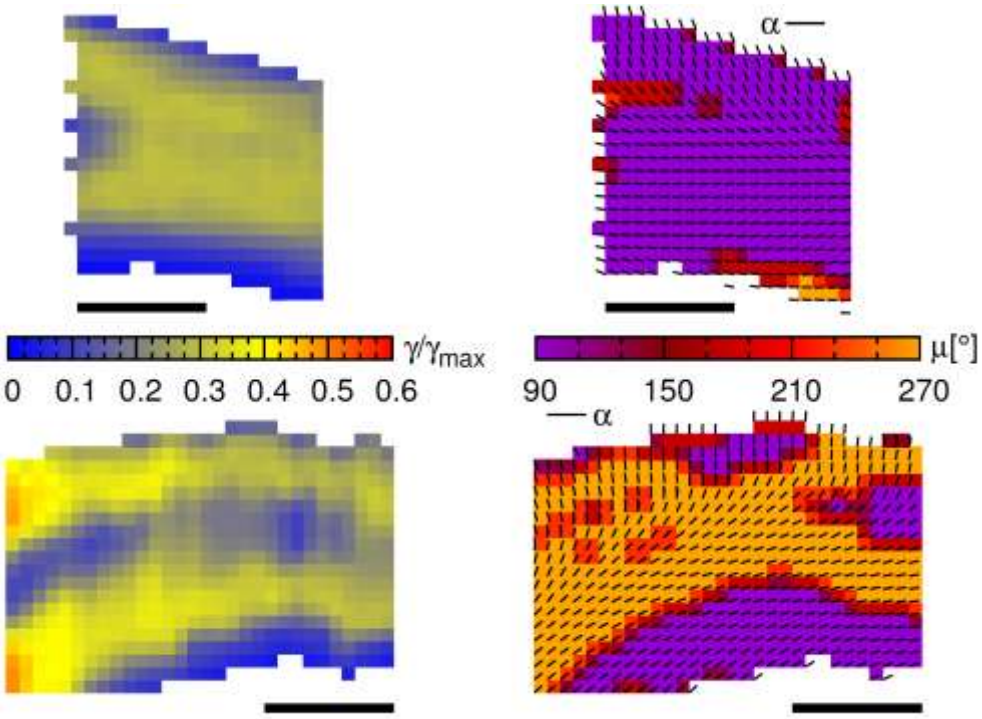

Figure S6: Texture of the chitin-fiber network. WAXS revealing the degree of orientational order relative to the maximal order within the sample γ/γ_{max} in terms the ratio of intensities of azimuthal peaks and the isotropic background, $\gamma=I_{peak}/I_{bgr}$ (left panel) and corresponding fiber texture (right panel) for two longitudinal sections of teeth, a) and b), respectively. In a) the tooth was cut further away from the tooth axis towards the surface. A comparison of fiber texture in a) and b) reveals also the presence of an out-of-plane texture. The scale bar is 100 µm.

S7. Details of the SAXS analysis – Structurally-limited power-law scattering

Theoretical background

In the Porod regime of q values, a particle surface can be considered to be locally flat and the particle shape and size is not important. For an ideally sharp planar interface, the scattering intensity scales as q^{-4}, which derives from the probability that any two points separated by a given distance r will be both in the bulk phase or the inner part of the surface phase – the so-

called Porod condition.[12] More generally, power law scattering is observed for mass-fractal, surface-fractal or diffuse interfaces.[13,14] The experimentally observed power-laws display structural limits in both, small- and high-q regimes, which are manifested in terms of regions of exponentially decaying scattering intensity.[12] Such behavior is interpreted as reflecting interfacial or mass-fractal scattering from a large structure in the low-q power-law regime composed of small-scale substructural units, whose mass- or surface-fractal scaling of the intensity is observed in the high-q power law regime.[12] The exponential region between two power laws reflects the average size of substructural units/particles.

In the regime of for small q (or equivalently large r), where r becomes similar to the particle size.[12] The power-law scaling therefore has a low-q limit beyond which it increasingly overestimates the scattering intensity. We therefore need to correct for the fact that a random placement of the first point will satisfy the Porod condition only with a certain probability, which leads to a so-called reduced q*.

The form factor of a centro-symmetric and rotationally averaged particle is defined as

$$\overline{F^2(q)} = 4\pi V {\rho_e}^2 \int_0^\infty g(r) \left[\frac{\sin(qr)}{qr}\right] r^2 dr, \quad (1)$$

where V is the particle volume, ρ_e is the electron density of the particle and g(r) is the so-called correlation function denoting the probability that a point located at a radial distance from a given point inside the particle will also be in the particle. The product $r^2g(r)$ is also called the distance distribution function p(r). The average structure in terms of a radially symmetric probability function is obtained by averaging of the scattering reference frame (i.e. the position of the first point) over all positions within the particle. Equivalently, we may consider the particle to diffuse randomly around the initial point resulting in a 3-dimensional Gaussian function centered at the initial point. However, for distances r approaching the

particle radius the random placement of the initial point will not always allow for fulfilling the Porod condition. More precisely, in some arbitrary direction given by a vector **r** from the initial point the maximal distance allowing the Porod condition to be fulfilled is *d* (see Fig. S6). We thus need to take into account only such 'allowed' displacements.

According to Ref. 5 the probability of finding two points separated by a distance r in the 'averaged' particle is hence

$$p(r) \propto exp(-3\,r^2/2\,\sigma^2), \tag{2}$$

where the variance is defined by

$$\sigma^2 = \left(\sum_{i=1}^{N}(x_i - \mu)^2\right)\Big/N \tag{3}$$

where **μ** is the position of the particle's center of mass and N is the total number of positions considered. Note that we omitted the normalization factor in Eq. (2) as we can introduce it at a later stage. For any **r** the second (end) point at location $\mathbf{x}_i$ must remain within the particle. If the origin of the vector **r** is at the centre of mass **μ,** the maximum particulate dimension in direction **r** is r_{max} and $d = r_{max}/2$. In *q*-space Eq. (2) corresponds to

$$p(q) \propto exp(-q^2\sigma^2/6). \tag{4}$$

To account for all possible allowed distances *d* we have to integrate Eq.(4) over all spheres of radius d=0 to $d = r_{max}/2$. This corresponds to integration over σ from 0 to σ_{max}, with

$$p(r) \propto exp(-3\,r^2/2\,\sigma^2), \tag{5}$$

$$\sigma_{max}^2 = \frac{\sum_k f_k {O_{\mu k}}^2}{\sum_k f_k} = R_g^2, \tag{5}$$

where f_k is the scattering factor for point *k* and $O_{\mu k}$ is the length of the vector from the centre of mass to the point *k* of an average particle and R_g is the radius of gyration of the particle. Upon a trivial change of variables the result of the integration is

$$\overline{p_1(q,R_g)} = \frac{2}{\sqrt{\pi}}\int_0^{qR_g/\sqrt{6}} \exp(-y^2)\,dy \equiv \mathrm{erf}(qR_g/\sqrt{6}), \tag{6}$$

where we now introduced a normalizing factor. To consider other orientations of the particle with respect to **r** and assuming that the other two dimensions are equivalent Eq. (6) is cubed, $\overline{p(q,R_g)} = \overline{p_1(q,R_g)}^3$. To account approximately for a finite structure of the particle we introduce the reduced q:

$$q^* = \frac{q}{\mathrm{erf}\left(\frac{qR_g}{\sqrt{6}}\right)^3}, \tag{7}$$

which enters Eq. (1) instead of q and leads to the corresponding structurally-limited power-laws $\overline{F^2(q)} \sim (q^*)^{-\alpha}$ that we have used in the analysis.

Structural limits also cause a systematic deviation of power-law scaling at high-q values, which is due to a finite average size of the scattering unit.[12,15] For example, a smooth interface cannot be considered smooth on the scale of chemical inhomogeneity and a polymer chain is not a continuous random curve below the persistence length. Below this length scale (for higher q) the scattering intensity decays exponentially (analogously to the Guinier's law) and thus gives rise to a multiplicative exponential cut-off to the reduced power law[12]

$$\exp\left(-R_{g,sub}^2 q^2/3\right), \tag{8}$$

with the sub-structural radius of gyration $R_{g,sub}$. Note that we have here the bare q. Moreover, the gyration radius of the structurally limited power law is equal to the (Guinier) radius of the particle, whereas the sub-structural radius corresponds to the (Guinier) size of the sub-structural particles/units. Moreover, for systems with several structural levels, and thus expectedly also for *M. crenulata*'s teeth, the respective exponentially cut-off effective power laws of the various structural level (particulate, subparticulate etc.) contribute independently to the scattered intensity.[12]

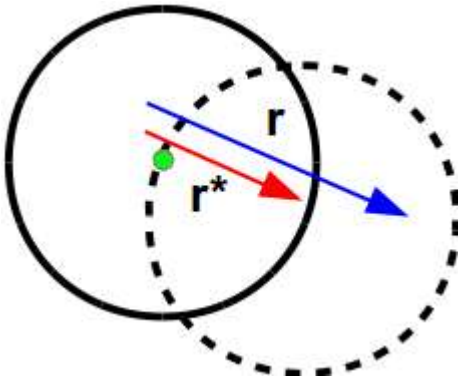

Fig. S7: Schematics of a violation of the Porod condition at small q. When |r| becomes comparable to the particle radius (with a center in the green dot), we need to correct for those occasions, where a virtual displacement of the particle in the direction **r** would result in a violation of the Porod condition. This results in a reduced distance r* or, after taking the Fourier transform, in a reduced q*.

Analysis of data

In agreement with the described theoretical concepts the results in Fig. S7.1 reveal the following scenario: generically, we find a structurally-limited and exponentially cut-off power law at small *q*, but the power depends on the location within the tooth. The effect of the transmitted beam and the limited low-*q* resolution prohibit a quantitative assessment of the Guinier radius of the largest scattering unit. At higher *q*, there appears to be a second (sub-structural) structurally-limited and exponentially cut-off power law, but the noise in the data does not allow for a quantitative assessment. We observe that small-scale scattering structures/interfaces (presumably corresponding to the sub-structural level) in the core extend to considerably higher *q*-values (compare Fig. S7.1 a1-a3 with Fig. S7.1 a4-a6). This means that the structural units in the core are built of smaller particles/units. While an accurate determination of the size of the smallest scattering units is limited by noise, we may estimate it from the high *q*-range, where the intensity falls off rapidly and obtain (d=2π/q) approx. 8-10.6 nm in the shell and approx. 4.-4.3 nm in the core. These smallest scattering units are

presumably proteins or protein aggregates. The observed power law is 4 in the shell and gradually drops to 2 in the core region. The shell region is thicker on the posterior side, which agrees well with SEM observations. The power 4 corresponds to the (structurally-limited) Porod law scattering from compact and sharp interfaces delimiting homogeneous compact phases.[12] The power 3 corresponds to scattering from mass-fractal associated networks or fractal surfaces and indicates a more open, fractal-interconnected and less compact structure.[13,14,16] Finally, the power 2 corresponds to scattering from Gaussian polymer chains, which indicates a completely open structure.[12,17] This is in good agreement with SEM observations (compare Fig. 2c-e in the main text). Thus, our results consistently demonstrate that the ultrastructure undergoes a gradual transition from compact to open as we move towards the tooth core (see also schematic in Fig. 3 in the main text). Moreover, comparing the scales of the basic scattering units in SAXS and the fibrous structures observed in SEM (Fig. 2c-2e), the latter evidently correspond to a higher level of structural organization, most likely to densely-packed bundles of proteins packed in-between chitin fibers, which cannot be resolved by SAXS due to the width of the transmitted beam.

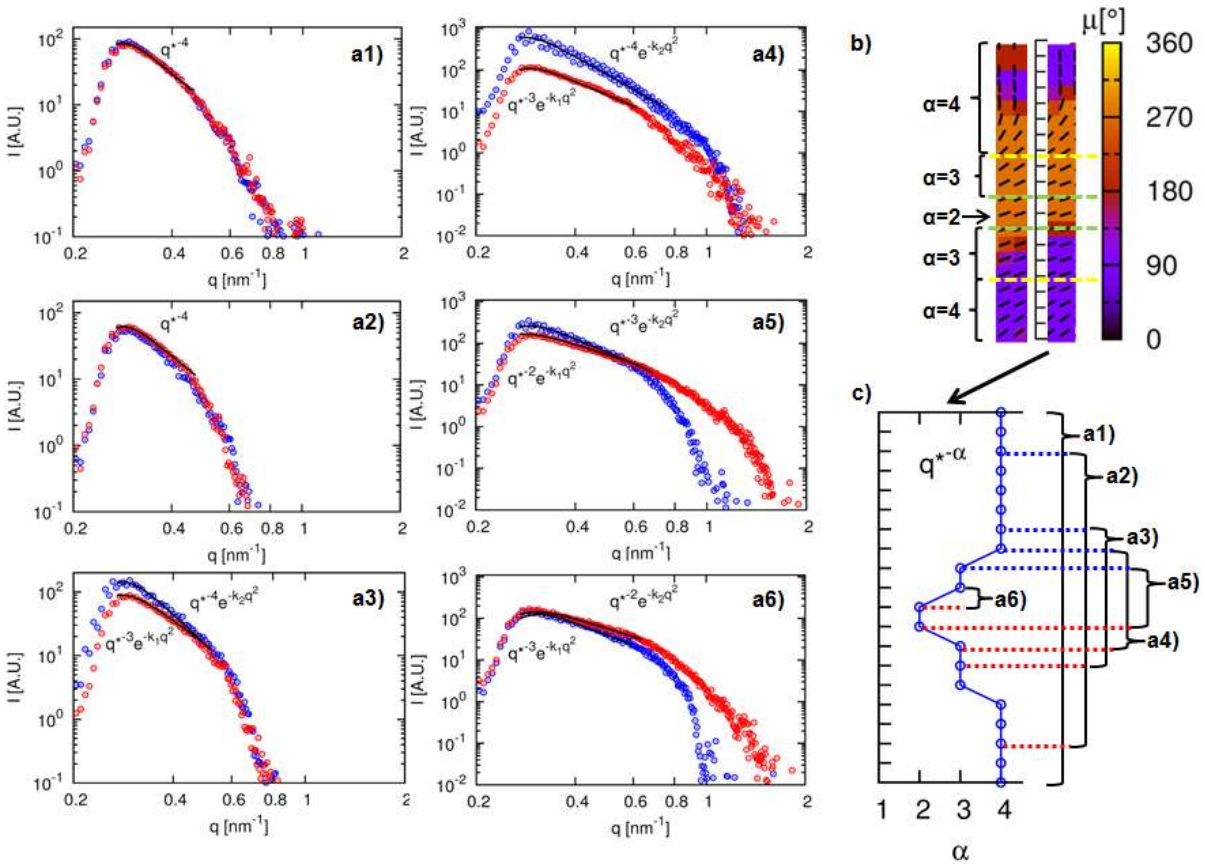

Figure S7.1: Packing of the fibrilar assembly. SAXS curves measured along the transverse section of the tooth (a1-a6) show results for every second measured point). b) Chitin texture within the region of interest, where the SAXS analysis was performed; overlaid are the grid points where SAXS measurements were performed. The intervals denote the obtained scattering exponents. c) The corresponding power α of the observed power-law $q^{*-\alpha}$ in the Porod regime along the grid of measurements depicted in b). The red and blue symbols in a1-a6 correspond to the red and blue lines in c). The symbol $q^* = q/\left[\mathrm{erf}\left(qR_g/\sqrt{6}\right)\right]^3$ corresponds to a reduced q - a mathematical correction for a particle with finite structure, where R_g denotes the effective average (statistical) particle radius of a given structural level[12]. Note that the exponential cut-off contains the bare q. d) Schematic of the ultrastructure in the core (α=2), transition region (α=3) and shell (α=4).

S8. Elemental composition of raw and EDTA-treated samples

The elemental maps of EDTA-treated samples are shown in Fig. S8 and compared to untreated samples. Treating the samples with EDTA removes from the very external surface layer most of the Mg and a substantial fraction of Ca ions (compare top and bottom lines of both panels, respectively).

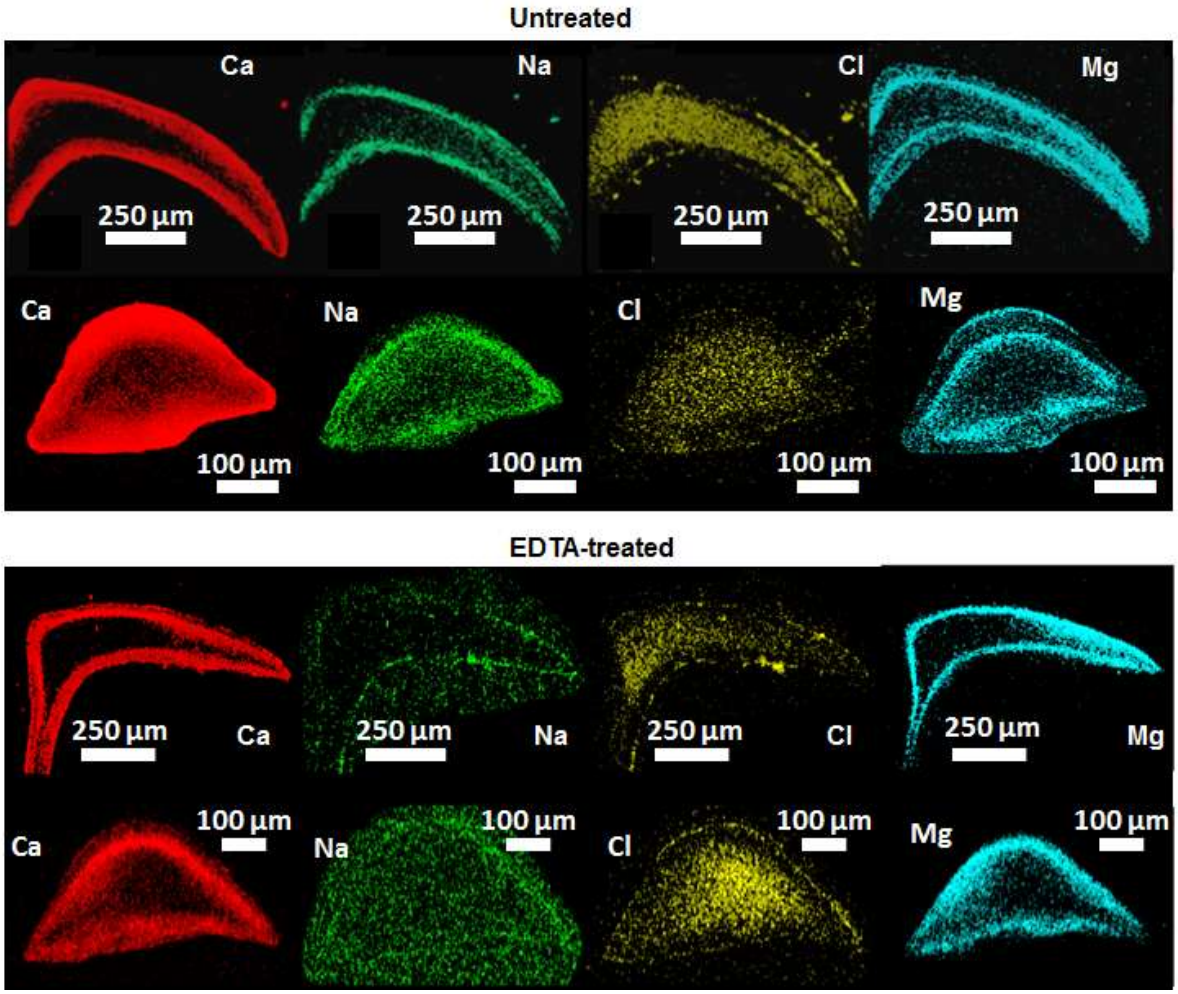

Fig S8: EDX Elemental maps. The figure depicts longitudinal and transverse sections of teeth for untreated (top line) and EDTA treated samples (bottom line).

S9. Presence of traces of Fe in extensively worn teeth

Using synchrotron-based X-Ray fluorescence we occasionally detected traces of Fe (a very weak signal) in extensively worn teeth (Fig. S9). We were not able to detect any Fe using EDX (not even in extensively worn teeth). Moreover, in mature but less worn teeth XRF did not reveal any Fe (there was no differences in the Fe content between the tooth and the environment). The Fe layer in extensively worn teeth is non-uniform and essentially app. one-pixel thick (~30 µm) and is missing in the tip, where the tooth is in contact with the substrate.

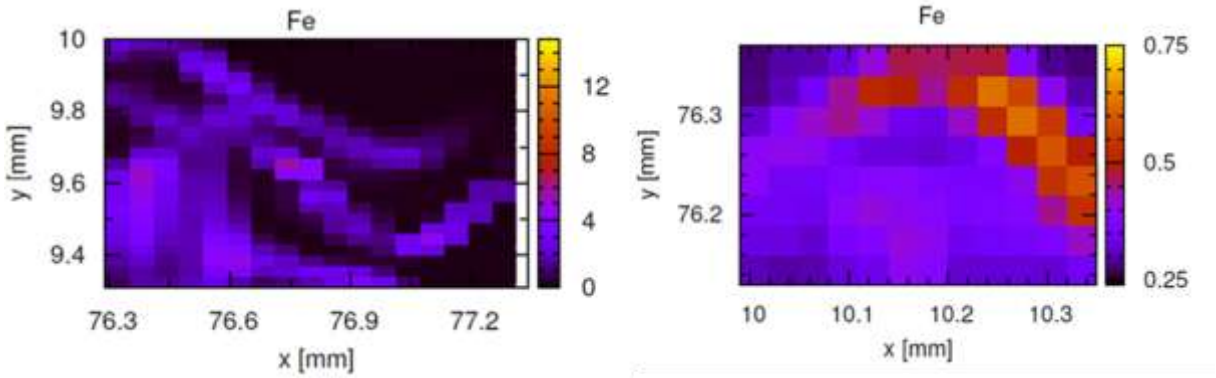

Fig. S9: X-Ray fluorescence map of Fe. XRF map of Fe of a longitudinal section of an extensively worn tooth.

S10. Hardness maps

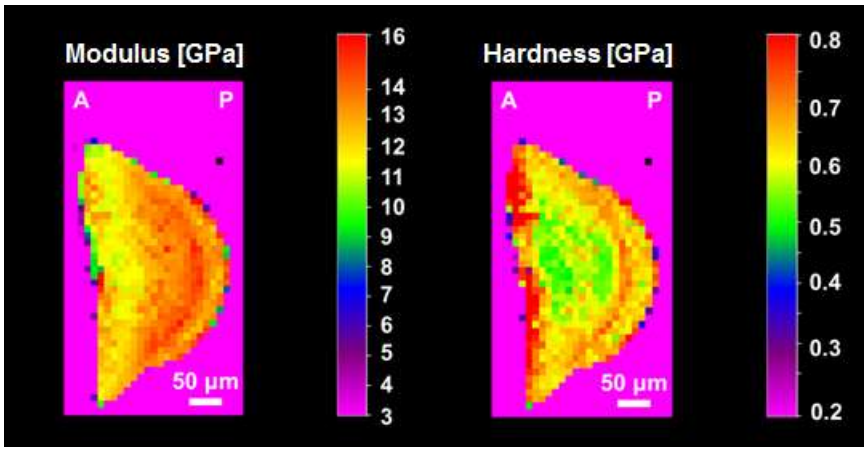

Fig. S10: Nanoindentation stiffness (left) and corresponding hardness (right) map.

S11. Effect of EDTA-treatment on the mechanical properties of teeth

In addition to partly removing Ca and Mg from the shell region the EDTA-treatment also caused changes in the mechanical properties. More precisely, the stiffer arch co-localized with Mg rich-layer disappeared (Fig. S11, left panel) and the stiffness in the surface layer decreased as well (compare with Fig. 1 in the main text and with Fig. S10). Most markedly, however, the hardness of the external region of the shell decreased from 0-7-0.8 GPa to app. 0.55 GPa (Fig. S11, right panel). This highlights a direct role of these cations for the stiffness and hardness of the teeth.

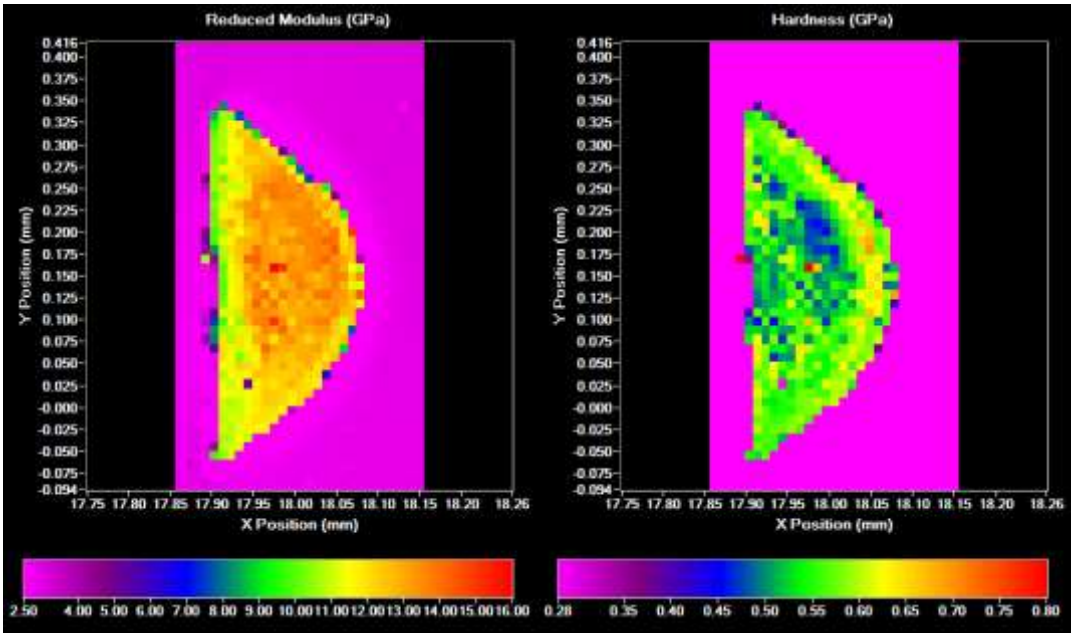

Fig. S11: Nanoindentation on EDTA-treated teeth. Modulus (left) and hardness (right) of teeth upon treatment with EDTA.

S12: Details of the data analysis

Microbeam SAXS and WAXS

The software DPDAK[18] was used for preparatory analysis of the 2-dimensional scattering data. Further analyses were performed with self-written software. Both the (040) and the (013) reflections were used to determine the local chitin content and texture. The difference in the results obtained from both reflections was within the statistical error but the (013) reflection was more visible and well resolved.

Nanoindentation

Load–displacement curves were analyzed for reduced modulus and hardness, using the method described by Oliver and Pharr[19] and the resulting reduced modulus and hardness data were plotted using XYZPlot (Hysitron).

Micro-tomography

Data reconstruction was carried out using the standard manufacturer reconstruction package (Nrecon, BrukerCT, Kontich, Belgium) and the reconstructed volumes were visualized in 2D (Fiji[20]) and in 3D (CTvox 2.6, BrukerCt, Belgium and Amira 5.2, Visage Imaging GmbH, Germany).

Scanning acoustic microscopy

The data was analyzed with SAM Process program (created by Puchegger Stephan).[8] With this program a time-dependent calibration curve was created to compensate a thermal drift of the voltage-reflectivity relation. The voltage values of the measured sample regions were then converted into reflectivity values R based on the time-dependent calibration curve.

References:

[1] T. Ukmar-Godec, G. Kapun, P. Zaslansky, D. Faivre, *J. Struct. Biol.* **2015**, *192*, 392

[2] A. Barth, *Prog. Biophys. Mol. Biol.* **2000**, *74*, 141.

[3] P. Geladi, H. Grahn, M. Manley, *Raman, Infrared, and Near-Infrared Chemical Imaging: Data analysis and chemometrics for hyperspectral imaging Ch. 5* (ed. Šašić, S. & Ozaki, Y.), 93-107 (John Wiley & Sons, Inc., Hoboken, New Jersey, 2010).

[4] E. A. Carter, H. G. M. Edwards, I*nfrared and Raman Spectroscopy of Biological Materials (Practical Spectroscopy): Biological Applications of Raman Spectroscopy Ch. 11* (ed. Gremlich, H. U. & Yan, B.), 421-475 (Marcel Dekker, 2001).

[5] J. L. Haston, S. B. Engelsen, M. Roessle, J. Clarkson, E. W. Blanch, C. Baldock, C. M. Kielty, T. J. Wess, *J. Biol. Chem.* **2003**, *278*, 41189 .

[6] T. Miura, T. Satoh, H. Takeuchi, *Biochim. Biophys. Acta.* **1998**, *1384*, 171.

[7] Y. A. Lazarev, B. A. Grishkovsky, T. B. Khromova, *Biopolymers* **1985**, *24*, 1449.

[8] S. Puchegger, D. Fix, C. Pilz-Allen, P. Roschger, P. Fratzl, R. Weinkamer, *J. Mech. Behav. Biomed. Mater.* **2014**, *29*, 438.

[9] H. Lichtenegger, M. Muller, O. Paris, C, Riekel, P. Fratzl, *J. Appl. Crystallogr.* **1999**, *32*, 1127.

[10] R. Seidel, A. Gourrier, M. Burghammer, C. Riekel, G. Jeronimidis, O. Paris, *Micron* **2008**, *39*, 198.

[11] O. Paris, M. Muller, *Nucl. Instrum. Meth. B* **2003**, *200*, 390.

[12] G. Beaucage, *J. Appl. Cryst.* **1995**, *28*, 717.

[13] P. Z. Wong, A. J. Bray, *Phys. Rev. Lett.* **1988**, *60*, 1344.

[14] H. D. Bale, P. W. Schmidt, *Phys. Rev. Lett.* **1984**, *53*, 596.

[15] W. Ruland, *J. Appl. Cryst.* **1971**, *4*, 70.

[16] J. Teixeira, *J. Appl. Cryst.* **1988**, *21*, 781.

[17] G. Porod, *Small-Angle X-ray Scattering (General theory)*, 17-51 (Academic Press, London, 1982).

[18] G. Benecke, W. Wagermaier, C. Li, M. Schwartzkopf, G. Flucke, R. Hoerth, I. Zizak, M. Burghammer, E. Metwalli, P. Müller-Buschbaum, M. Trebbin, S. Förster, O. Paris, S. V. Roth, P. Fratzl, *J. Appl. Cryst.* **2014**, *47*, 1797.

[19] W. C. Oliver, G. M. Pharr, *J. Mater. Res.* **1992**, *7,* 1564.

[20] J. Schindelin, I. Arganda-Carreras, E. Frise, V. Kaynig, M. Longair, T. Pietzsch, S. Preibisch, C. Rueden, S. Saalfeld, B. Schmid, J. Y. Tinevez, D. J. White, V. Hartenstein, K. Eliceiri, P. Tomancak, A. Cardona, *Nat. Methods* **2012**, *9*, 676.
[21] D. K. Padilla, *Marine Biol.* **1985**, *90*, 103.
[22] Y. Tan, S. Hoon, P. A. Guerette, W. Wei, A. Ghadban, C. Hao, A. Miserez, J. H. Waite, *Nat. Chem. Biol.* **2015**, *11*, 488